

Sequestration of Ca in simian nasal mucosa: Determination of Ca molarity in ex vivo tissue by simultaneous off-axis Scanning Transmission Ion Microscopy, Particle Induced X-Ray Emission and Elastic Backscattering Spectrometry

Harry J. Whitlow^{a,b,d,e,*}, Gyula Nagy^c, Nicholas Henderson^{d,e,1}, Richard Greco^d, Naresh Deoli^{d,e,2}, Karen M. Smith^f, Karen Morgan^g, Francois Villinger^g

^a Tandem Laboratory, Uppsala University, PO Box 529, Uppsala, SE-751 21, Sweden

^b Department of Physics, University of Oslo, Blindern, Oslo, N-0316, Norway

^c Department of Physics and Astronomy, Uppsala University, PO Box 516, Uppsala, SE-751 20, Sweden

^d Louisiana Accelerator Center, University of Louisiana at Lafayette, P.O. Box 43680, Lafayette, LA 70504, USA

^e Department of Physics, University of Louisiana at Lafayette, P.O. Box 43680, Lafayette, LA 70504, USA

^f Department of Biology, University of Louisiana at Lafayette, P.O. Box 43602, Lafayette, LA 70504, USA

^g New Iberia Research Center, University of Louisiana at Lafayette, P.O. Box 13610, New Iberia, LA 70562, USA

ARTICLE INFO

Keywords:

MeV Ion Microprobe

Off-axis Scanning Transmission Ion Microscopy (STIM)

Particle Induced X-ray Emission (PIXE)

Elastic Backscattering Spectrometry (EBS)

Nasal mucosa

Ca sequestration

Simian Immunodeficiency Virus (SIV)

ABSTRACT

A technique to determine the molar concentration of elements in ex vivo tissue sections by Particle Induced X-ray Emission (PIXE) has been developed. The method is based on simultaneous off-axis scanning transmission ion microscopy (OA-STIM) and Elastic Backscattering Spectrometry (EBS) measurement of the sample thickness and major element (H, C, N, O) composition. The method was applied to determine the molarity of localised Ca concentration hot-spots in the outer epithelium tissue of nasal mucosa of a rhesus macaque subject infected with simian immunodeficiency virus (SIV). The results show Ca sequestration in concentration hot-spots and outer epithelial tissue that significantly exceeded the Ca concentration in the surrounding tissues. This may originate from mineralisation and/or Ca enhancement in goblet cells.

1. Introduction

Of the 92 naturally occurring elements, 23 are life elements which are physiologically important [1,2]. In humans [3], major life elements (H, C, N, O) make up 96 mass %, lesser life elements (Na, Mg, Si, P, S, Cl, K, Ca, Fe and I) < 3.9 mass % and trace elements (F, Si, V, Cr, Mn, Co, Ni, Cu, Zn, As, Se, Br and Mo) < 10 mass ppm. Meaningful physiological concentrations of substances in the life sciences are generally expressed in terms of molarity for in vivo tissue. Typically, the levels range from pmol dm⁻³ to tens of mmol dm⁻³. The trace elements such as Fe, Cr, Mn, Cu and Zn are often incorporated in proteins where they determine the shape and hence the functional behaviour of the protein.

1.1. Ca in biological tissue

The life element investigated here is Ca, which has a remarkably wide range of concentrations in biological matter. This ranges from a

total Ca intracellular level of ~100 nmol. dm⁻³ [4] to ~9.7 mol. dm⁻³ calculated from ICRU tissue composition data [5] for cortical bone tissue. From Ref. [6] the calculated total molarity of Ca in blood and a representative soft tissue (tongue) was 0.64 and 0.14 mmol. dm⁻³, respectively. At the intracellular level about half is present as Ca²⁺ and the rest is bound in proteins [4]. Bound Ca can be deposited in the inter-cellular matrix as mineralisation. e.g. as calcium hydroxyapatite, Ca₁₀(PO₄)₆(OH)₂ in bone tissue. Cellular regulatory systems maintain homeostasis between bound-Ca and Ca²⁺ [3,7–10]. Ca²⁺ participates in a number of inter- and intra-cellular signalling processes. For example it acts as a signal substance for apoptosis, muscle contraction, hormone release, inflammation, immune system response and, of particular relevance here, the release of mucus from granulae in the goblet cells of mucosa [11,12]. It follows from its importance as a signal substance

* Correspondence to: Department of Physics, University of Oslo, Blindern, N-315, Oslo, Norway.

E-mail address: HarryWhitlow@fys.uio.no (H.J. Whitlow).

¹ Present address: Louisiana State University Health Shreveport, Shreveport, LA 71103, USA.

² Present address: Columbia University, Center for Radiological Research, New York, NY 10032, USA.

that local Ca element concentrations in tissues may be altered as a result of infection, inflammation and tissue remodelling (as for Cu [13]). This is likely to be particularly true of mucosal tissues because this is the site of the immune system's first line of defence against infection.

Our interest in spatial perturbation of trace element concentrations stems from work by one of us (FV) on Simian Immunodeficiency Virus (SIV) which is used as a model for HIV-research. This study used positron emission tomography (PET) imaging with immunological markers labelled with ^{64}Cu to show that SIV is localised in different organs in the body as the infection develops [14]. It is then interesting to see if we could use trace elements measured using PIXE with a MeV ion microprobe to extend this down to the tissue elemental level.

1.2. Ion beam analysis of biological tissue

Particle Induced X-ray Emission (PIXE) using a MeV ion microprobe is well suited to simultaneously measure low concentrations of trace life elements [2]. As noted above, bound Ca in tissues can be deposited by calcification. Conventional histological stains for calcification (von Kossa and Alizarin Red S [15]) are not Ca-specific but stain by pigment deposition in response to a number of different mineralisations. Analysis with a MeV ion microprobe using PIXE has the advantage that not only is the measurement Ca-specific, but also colocalisation of other elements like Mg, Si, Fe and P can provide even more specific detail on the calcifying mineralisation.

In ion beam analysis the elemental contents are expressed in terms of basic units of atoms per unit area. For PIXE where the major element content and thickness of the sample is known, the standard software analysis codes use tabulated data and generally express the elemental content as a dry mass ppm ratio. This parameter is of limited biological significance since it is poorly representative of in vivo tissue. Here we report development of a procedure to determine the elemental molarity in tissue sections of ex vivo tissue which is a biologically more pertinent quantity than the elemental dry mass ppm ratio.

Reported work in the literature used the on-axis (Direct-STIM)/off-axis Scanning Transmission Ion Microscopy (STIM) approach to assign a thickness in terms of mass per unit area without knowledge of major element composition [16,17]. This is inadequate for quantitative biological analysis because the stopping is governed in biological samples by the major element composition. For example, significant changes in major element composition can be seen in Fig. 2 of [18] where comparing the contrast seen in the on-axis (energy loss) and off-axis (H-map) images reveals that significant quantities of hydrogen was present even in regions with low-energy loss. The major elements (H, C, N and O) in biological samples contribute leading terms to the ion energy loss as well as the absorption of X-rays in the sample, both of which are key parameters in PIXE analysis. *It follows that in order to make accurate determinations of the content of lesser- and trace-elements by PIXE in dry tissue samples both the thickness and major element composition must be determined.*

Another consideration is water loss. In vivo human tissues contain 65–80 mass % water [3]. Consequently, the degree of water loss will significantly influence the major element composition of the dry tissue as illustrated in Fig. 1 which is based on data from Ref. [6]. Furthermore, the amount of water lost may depend on the particular type of tissue. It turns out that for determining the molarity from the PIXE data analysis requires the major elemental composition and thickness of the dry tissue as well as the thickness of the ex vivo tissue section. Cast in this way, the determination of the measured molarity is independent of the amount of water and other major elements lost during lyophilization of the ex vivo tissue.

Measurement of H and other light element contents of aerosols deposited on a hydrogen-free substrate of uniform thickness, such as PTFE can be carried out by broad-beam Proton Emission Scattering Analysis (PESA). Off-axis Scanning Transmission Ion Microscopy (OA-STIM) is similar to PESA [19–21], but adapted to the case where the thickness and composition varies over the sample.

The present work is based on the use of OA-STIM and Elastic Backscattering Spectrometry (EBS) to measure the major element (C, H, N and O) composition and tissue section areal density simultaneously with PIXE measurements of Ca. Combining the Ca to matrix dry mass ratio from PIXE and the areal density and composition from EBS/OA-STIM data yielded the mass density of Ca in the film. This was then scaled according to the microtome slice thickness to obtain a molarity for Ca that corresponded to the ex vivo tissue.

2. Experimental

2.1. Microprobe analysis

Analysis was carried out at the Louisiana Accelerator Center [22] using a microprobe set-up with 2 MeV H^+ ions. This employed a conventional Oxford quadrupole triplet configuration lens system which allowed focusing the beam to a spot size of 1–2 μm on the sample. The sample was mounted on a motorised X–Y–Z stage. The configuration is shown in Fig. 2. The X-ray detector is internally collimated to 50 mm^2 active area and the detector window is 12.5 μm of Be and a 62.5 μm Mylar[®] filter. The off-axis STIM detector was operated without a stopping foil. A conventional Oxford Microbeams OMDAQ data acquisition system was employed using a OM-1000e interface. The magnetic scanning was driven by Kepco BOP 100-4 programmable power supplies. This set-up allowed the OA-STIM, PIXE and EBS spectral data to be collected simultaneously into a sequential event mode data file. The image data was collected with 512 pixels \times 512 pixels resolution. Supplementary measurements were conducted at the MeV Ion Microprobe Facility at the Tandem Laboratory, Uppsala University [23].

The energy calibration of the X-ray detector was determined using a thick Au sample using PIXE to produce $\text{Au L}\gamma_1$ (13.382 keV) and $\text{M}\alpha$ (2.123 keV) characteristic X-rays. The EBS detector was calibrated from the position of the high energy edge using the same Au sample and the narrow ^{16}O EBS backscattered ion peak from the thin Pioloform region (discussed below). The peak from H in the same Pioloform film was used for a single point calibration of the off-axis STIM detector with linearity controlled using a pulser. The MeV ion microprobe scan size was calibrated using copper electron microscope grids with a pitch that had been calibrated using a scanning electron microscope against a wire of precisely known thickness.

2.2. Spectrum and elemental map data analysis procedure

The GeoPIXE code [24–26] was used to process the event mode data files to produce EBS and ERDA energy spectra from specific regions of interest in the sample images as well as PIXE elemental maps for the different elements in the sample. This code was used because the background-free Direct Analysis fitting facilitated separation of elemental maps from the overlapped PIXE signals from $\text{K K}\beta$ and $\text{Ca K}\alpha$ characteristic X-rays. This is important for biomedical samples because both K and Ca are lesser elements that have characteristic X-rays with energies that partially overlap.

The EBS and OA-STIM energy spectra corresponding to the different tissue regions of the sample were analysed using a purpose-built Python fitting programme. Using this code the position of the high energy edge and area of the OA-STIM H-signal were measured. The code was also used to measure surface edge heights corresponding to C, N and O in the EBS spectrum. This was done by non-linear fitting the sum of functions representing the contributions to the EBS signals for each element. These functions were the product of $\text{erf}(x_1)$ and $\text{erf}(x_2)$ functions with a trapezoid representing an edge height and slope. The edge heights, edge positions x_1 and x_2 , edge widths and slopes were fitting parameters.

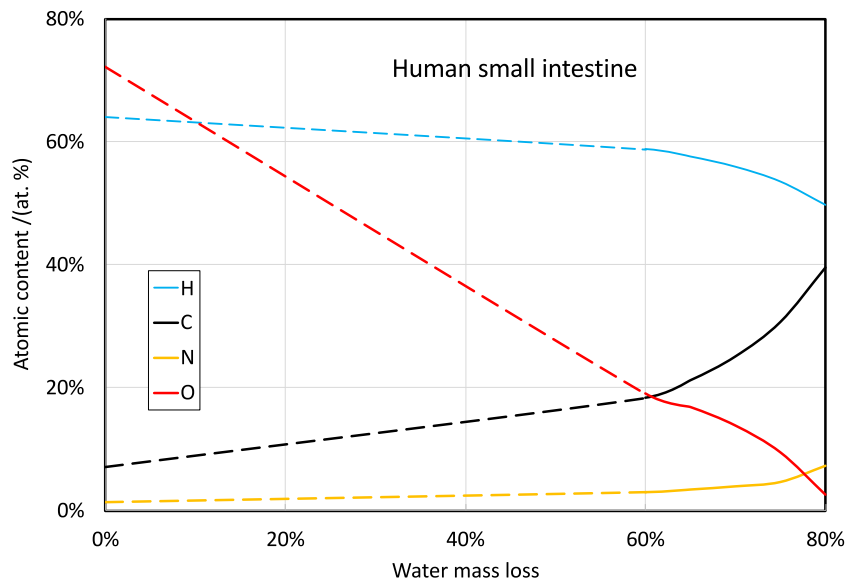


Fig. 1. Calculated major element composition against percentage of mass-loss in dehydration. The in vivo tissue composition was taken from Ref. [6] and converted to mass %.

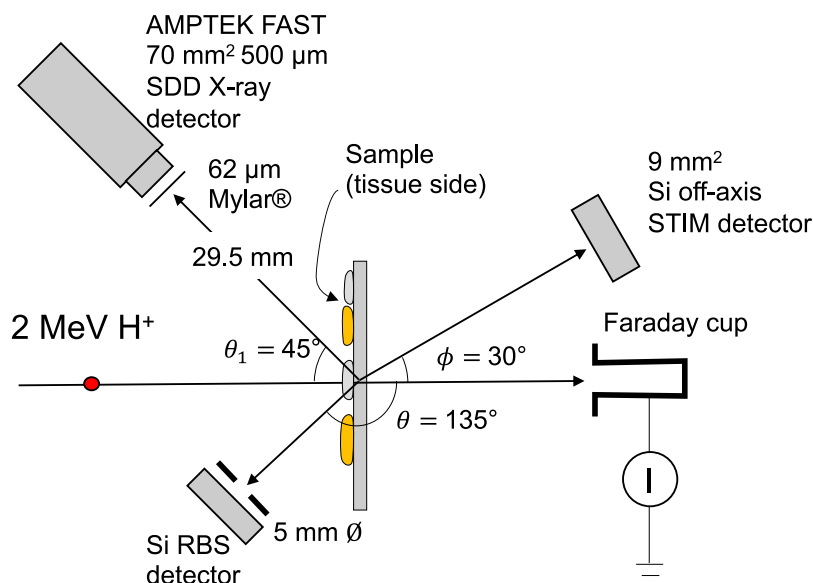


Fig. 2. Schematic illustration of the microprobe setup at the Louisiana Accelerator Center.

2.3. Tissue preparation

For this study ex vivo nasal mucosa samples were taken during necropsy of a rhesus macaque (*Macaca mulatta*) subject. This animal had been used in another study that was approved by the Institutional Animal Care and Use Committee (IACUC) of the University of Louisiana at Lafayette. (No approval was required for this study as the samples were taken post-mortem.) The subject was a 9 year old male that had been infected for a period of 4 years with Simian Immunodeficiency Virus (SIV) (SIVmac239). As the goal of the study was to determine the element distributions in the tissues, care was taken not to introduce foreign elements during preparation. For this reason chemical fixing was not used [27]. The animal was euthanised using an approved method [28] by pentobarbital injection. The samples were taken at necropsy and wiped with clean tissue paper during grossing to remove extraneous fluids without water rinsing. Subsequently they were embedded in Optimal Cutting Compound (OCT) [29] and frozen by

cooling to -80°C . The samples were sectioned in a cryomicrotome and the $10\text{ }\mu\text{m}$ film transferred to supporting Pioloform® films supported on 5/16" stainless steel washers. The Pioloform films were prepared following Ren's protocol [30] by dipping clean microscope slides in a solution of Pioloform in chloroform and floating the film off on the surface of deionised water. Subsequently, the Pioloform films were picked up on the washer.

3. Formalism

Quantitative interpretation of OA-STIM energy spectra is more intricate than conventional stopper-foil, glancing angle ToF-E ERDA [31,32] and EBS [32,33] energy spectra. This originates from the transmission geometry. Moreover, where the projectile and target atoms are the same (e.g., p-p, $^4\text{He} - ^4\text{He}$ scattering) the cross sections are non-Rutherford. For brevity and completeness only a brief description is given here.

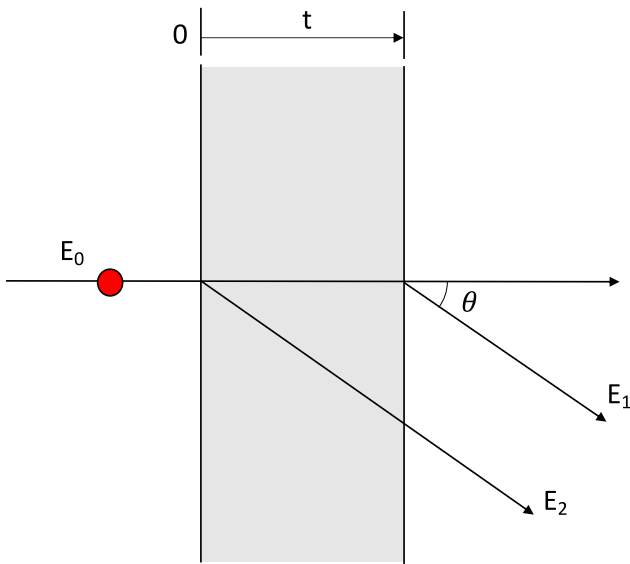


Fig. 3. OA-STIM scattering geometry.

3.1. Off-axis STIM

For the geometry illustrated in Fig. 3, where K is the kinematic factor and ϵ_{in} the stopping cross section along the inward path in a thin sample is:

$$E_1 = KE_0 - Nt(K\epsilon_{in}) \quad (1)$$

and,

$$E_2 = KE_0 - Nt\left(\frac{\epsilon_{out}}{\cos\theta}\right) \quad (2)$$

Then, the stopping cross section factors $[\epsilon]$ are given by,

$$\Delta E_1 = E_1 - KE_0 = Nt[\epsilon]_1 = -Nt(K\epsilon_{in}) \quad (3)$$

$$\Delta E_2 = E_1 - KE_0 = Nt[\epsilon]_2 = -Nt\left(\frac{\epsilon_{out}}{\cos\theta}\right). \quad (4)$$

The subscripts 1 and 2 refer to scattering from the faces of the samples on which the ion beam respectively egresses and impinges (Fig. 3). For Bethe-like stopping above the stopping maximum, $\Delta E_1 \leq \Delta E_2$, because K and $\cos\theta$ are both < 1 . The implication is that, unlike the glancing angle ERDA and EBS cases; (i) the high energy edge in the OA-STIM energy corresponds to the exit surface of the sample, (ii) both the front and back surface energies move to lower energies with increasing sample thickness Nt and (iii) As Nt increases the difference in edge energies $\Delta E_1 - \Delta E_2$ is a fraction (< 1) of ΔE_1 . Note that (ii) and (iii) imply that, unlike EBS and ERDA, both the position and shape of the OA-STIM peak are influenced by sample thickness variations. Thickness variations in our biological samples therefore confounded the quantitative analysis of the OA-STIM hydrogen signal. Notwithstanding this, it was found that the areal density of H could be obtained from the yield under the H-peak in the OAS signal and the thickness of the dry tissue film could be measured using Eq. (3) from the energy shift of the high energy edge of the H signal.

3.2. Major element atomic compositions and thickness

The underlying idea in the measurement of the major element composition of the dry tissue film was to determine the elemental contents from the edge heights corresponding to H, C, N and O using a modified version of the standard EBS formalism [32,33].

It is straightforward to use the standard EBS formalism [32,33] to determine the relative contents of C, N and O from the surface edge

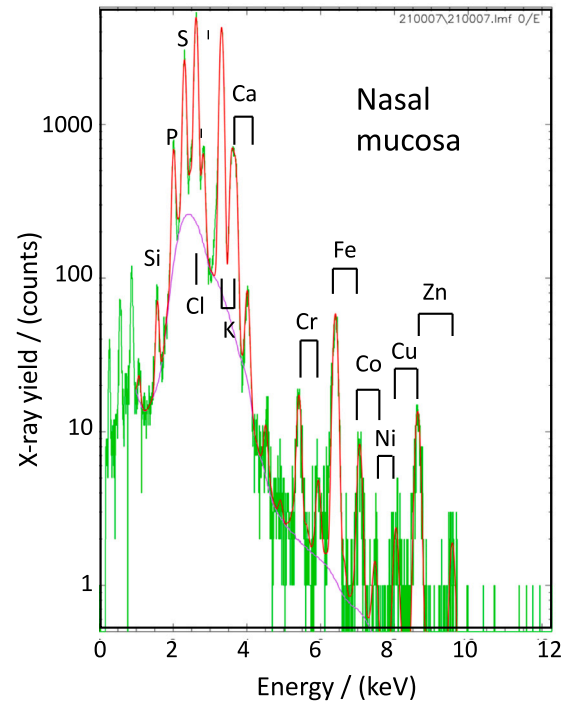


Fig. 4. PIXE X-ray spectrum from tissue region 4 (lamina propria) measured with 2 MeV protons. Key: green: measured spectrum, red: fitted spectrum, purple: background.

heights in the backscattered spectrum, even though the differential cross-sections are non-Rutherford [34–36]. In this way the ratios of the number of nitrogen and oxygen to carbon atoms n_N/n_C and n_O/n_C can be determined. This used the differential scattering cross-sections from SigmaCalc [37,38] and the molecular stopping cross-sections from DPASS [39,40] in conjunction with Bragg's rule.

Similar to the EBS case [33], the H to C atomic ratio was obtained from,

$$\frac{n_H}{n_C} = \frac{Y_H E_{ch} [\epsilon]_H}{h_C \Delta E_1 [\epsilon]_C Y}, \quad (5)$$

where, the subscript H denotes parameters pertaining to the OA-STIM measurement of H and subscript C denotes parameters for backscattering of carbon. Y_H is the area under the OA-STIM H peak. (A small correction for H yield from the supporting Pioloform film was applied to Y_H by subtracting the yield from the Airway region (where no tissue is present) scaled according to the number of pixels in the two areas.) h_C is the surface edge height of the backscattered carbon signal. E_{ch} is the energy per channel in the backscattering spectrum. The $[\epsilon]$ terms are the stopping cross-section factors for OA-STIM (e.g. Eq. (3)) and backscattering [33], respectively. The parameter, Y accounts for the non-Rutherford scattering cross-sections, for forward scattering of protons from H and backscattering of protons from C [34,43] as well as the subtended solid angle ratio for the OA-STIM and backscattering detectors. Here, η was determined according to,

$$Y = \frac{Y_{H_0} n_{C_0}}{Y_{C_0} n_{H_0}}. \quad (6)$$

Y_{H_0} was the OA-STIM H yield, Y_{C_0} the backscattered yield for p-C scattering for a thin standard (~ 500 nm Pioloform) with a known H to C ratio (n_{H_0}/n_{C_0}) [44]. The standard should be sufficiently thin that the H and C signals are sharp peaks. This approach, which is similar to the PESA case, has the advantage that it does not require a priori knowledge of the scattering cross-sections nor measurement of the detector solid angle ratio.

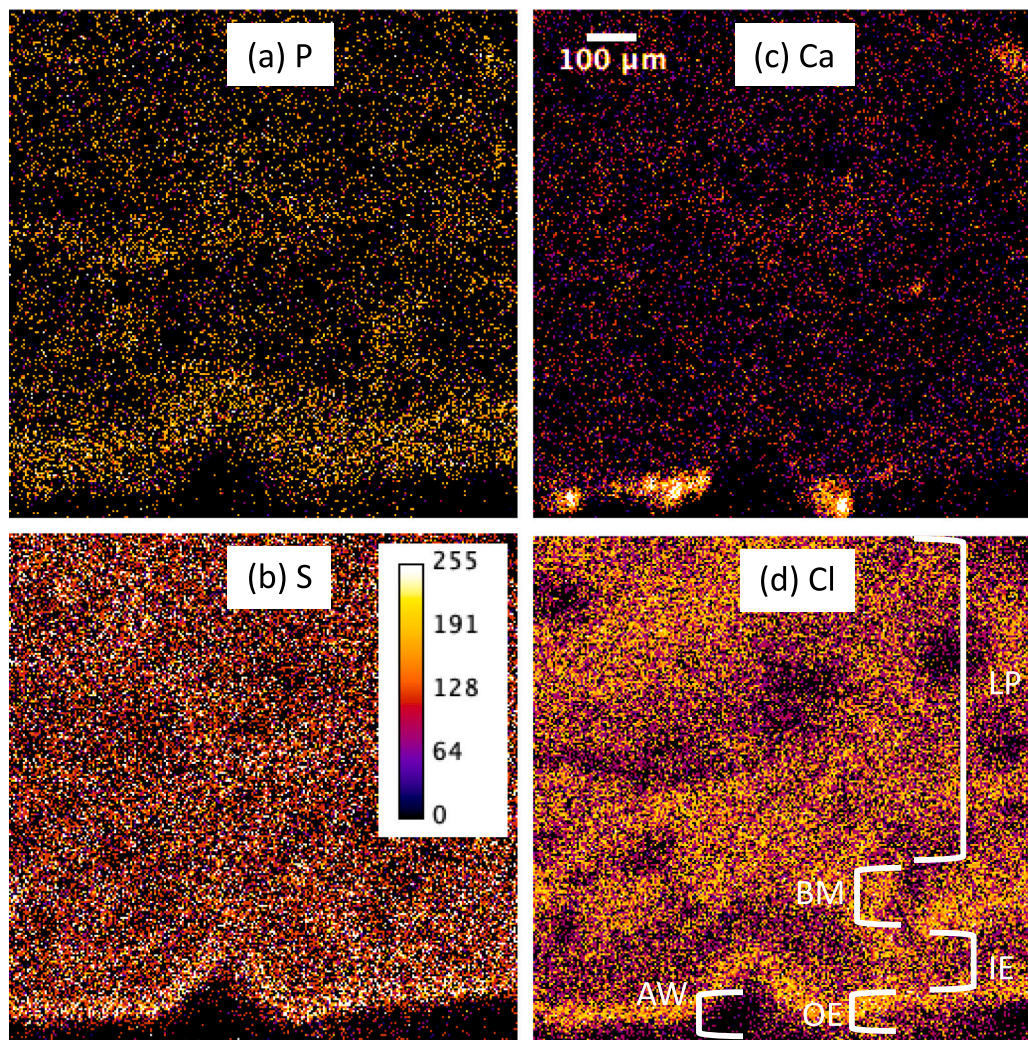


Fig. 5. Normalised PIXE images; (a) P, (b) S, (c) Ca and (d) Cl. Key: AW: airway, OE: outer epithelium, IE: inner epithelium, BM: basal membrane, LP: laminar propria. The histological tissue identification is based on [41,42]. Note: the images have been contrast-normalised to improve visibility. The colour pallet in (b) denotes the contrast normalised relative X-ray yield.

3.3. Calculation of molarity

The major element composition and film thickness were used as input data in the analysis of the PIXE spectra using GeoPIXE to obtain the dry mass ratio M_i/M_{matrix} , where M_i is the mass of the element in question (Ca). The average atomic mass of the matrix is M_{matrix} . This is calculated from the major element composition determined by EBS and OA-STIM, as described above. Combining this with the areal density of the tissue section (Nt) from ΔE_1 and the thickness T of the ex vivo tissue section gives x the number of moles per unit volume.

$$x = \left(\frac{M_i}{M_{matrix}} \right) \left(\frac{M_{matrix}}{TA_i} \right). \quad (7)$$

This can be expressed as a molarity by scaling to a volume of 1 dm³.

4. Results and discussion

A PIXE X-ray spectrum from the region of the tissue section that corresponded to the laminar propria is shown in Fig. 4. This showed that X-ray signal from life elements P, S, Cl, K, Ca Cr, Fe, Co, Ni, Cu and Zn were observed. No disturbing background from other elements was observed. Fig. 5 shows the P, S, Ca and Cl PIXE elemental maps from the nasal mucosa section. The other PIXE elemental maps were

unremarkable. The different tissue regions have been identified in Fig. 5(d) based on Refs. [41,42]. Comparison of Fig. 5(a) and (b) showed that P and S in the epithelial region exhibited two layers. A 150–200 μm thick inner epithelium layer where P is enhanced that is visible in Fig. 5(a) and a 40–60 μm thick outer epithelium layer with enhanced S seen in Fig. 5(b). Significant local enhancement of Ca was observed in circular concentration “hot-spots” of 20–50 μm within the outer epithelium region. (Lower part of Fig. 5(c).) It was remarkable that the Ca signal in the “hot-spots” significantly exceeded that of the surrounding tissues.

4.1. Determination of the Ca molarity

To determine the Ca molarity in the hot-spots and surrounding tissues, spatial regions of interest were defined based on the PIXE elemental maps. These regions were used to delineate the different types of tissue in Fig. 5(d). These regions were (i) the airway, (ii) outer epithelium with Ca hotspots, (ii) outer epithelium without Ca hotspots, inner epithelium, (iii) basal membrane (iv) lamina propria and (v) four Ca hot-spots (Ca HS 1 – Ca HS 4). The total hydrogen yield map from OA-STIM is shown in Fig. 6(a) with tissue regions shown in Fig. 6(b). Fig. 7 shows the normalised hydrogen OA-STIM energy spectra corresponding to the different tissue regions identified in Fig. 6.

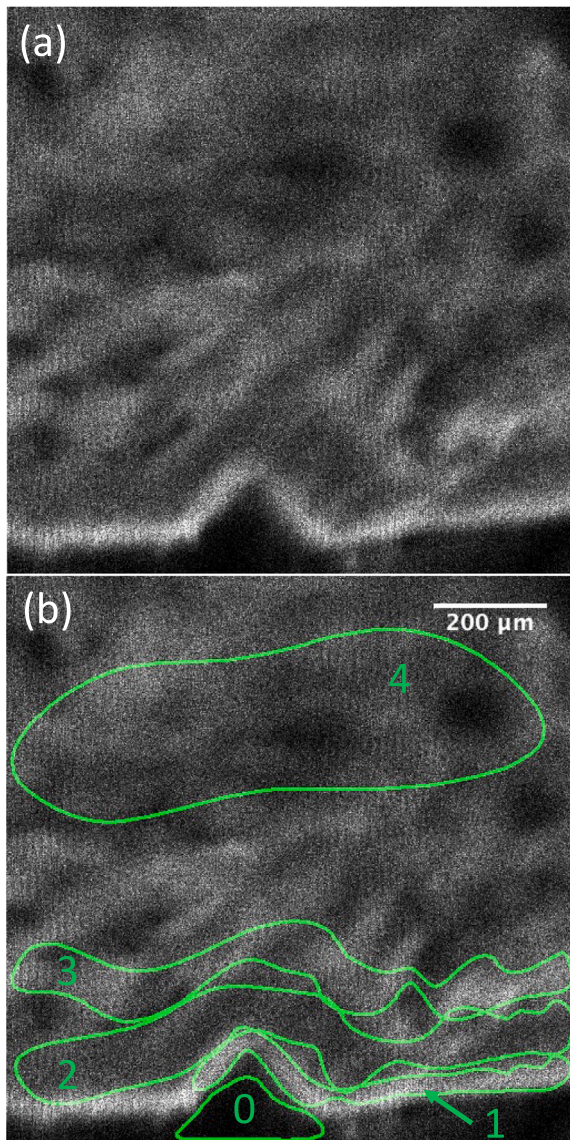


Fig. 6. (a) Total hydrogen grey scale yield map from OA-STIM. (b) Regions corresponding to different tissue types. Key: 0: Airway; 1: outer epithelium, 2: inner epithelium, 3: basal membrane, 4: lamina propria.

As noted above, energy shifts and energy broadening associated with sample thickness variations within each analysed region confounded the OA-STIM analysis. Therefore ΔE_1 was used to determine the section thickness because comparing Eqs. (3) and (4) showed that this parameter was the least susceptible to roughness and thickness variations. The total H yield Y_H for each tissue region was taken to be the yield under the H-peak after subtracting a small correction for the yield from the Pioloform supporting film. A similar small correction was applied to the energy loss ΔE_1 (Section 3.1). ΔE_1 was determined from the energy displacement of the high energy side of the H peaks at 50% height, (Fig. 7).

The relative C, N and O contents in the tissue section were then determined from the EBS spectra for each region by fitting the high energy edges corresponding to the C, N and O surfaces. The result of such a fit is illustrated in Fig. 8. The factor η (Section 3.2) was determined using the Pioloform in the airway region (See Fig. 5(d)) where no tissue was present as an internal standard with composition 31.52 at.% C, 57.88 at.% H and 10.60 at.% O. The 2 MeV proton fluence of 3.8×10^{14} protons cm^{-2} was expected to introduce an insignificant

Table 1

Dry major element composition and counting statistical uncertainties for the different tissue regions in Fig. 5.

Tissue	H at.%	C at.%	N at.%	O at.%	t/(μm)
AW	58.16	32.64		9.20	0.172 ± 0.002
OE	67.77 ± 5.56	18.70 ± 1.95	5.11 ± 1.21	8.42 ± 1.21	5.40 ± 0.11
IE	65.55 ± 2.64	21.06 ± 1.07	5.28 ± 0.64	8.11 ± 0.64	2.83 ± 0.06
BM	64.52 ± 3.42	19.67 ± 1.33	8.40 ± 0.79	7.42 ± 0.79	3.83 ± 0.08
LP	55.22 ± 2.93	29.00 ± 1.97	5.97 ± 0.70	9.82 ± 0.70	2.70 ± 0.05
Mean	63.26 ± 1.66	22.11 ± 0.69	6.19 ± 0.35	8.44 ± 0.35	4.91 ± 0.05

composition change in the internal standard [44]. This was confirmed in supplementary measurements with 2 MeV protons using the Uppsala Microprobe Facility [23]. The PEG (polyethylene glycol) and the water content of OCT compound [29] was assumed to have been lost during drying and vacuum pumping.

The dry tissue major element compositions and thickness were then calculated for each tissue region. The major element composition was used to convert the energy loss into a thickness by iteration. The usual zero-order assumption for EBS that the ratio of the stopping cross sections $[\epsilon]_i / [\epsilon]_j \approx 1$ was not applicable when determining the n_H/n_C using Eq. (5). Instead, the zero-order stopping cross sections for hydrogen were based on a hydrogen atomic content of 55.93 at.% which was calculated for small intestine tissue [6] with 70 mass % water loss. Table 1 and Fig. 9 present the dry tissue data after the second iteration. The geometric thickness was calculated assuming a dry tissue density of $1.361 \times 10^3 \text{ kg m}^{-3}$. (This value corresponded to rat heart tissue [45]. The densities of ex-vivo human soft-tissues [6] are within $\sim 5\%$ that of rat heart tissue suggesting this value of dry tissue density will be close to that for soft tissues in general.)

The data in Fig. 9 and Table 1 showed that the atomic contents of H, C, N and O varied from one tissue region to another. The error bars represent statistical counting uncertainties. The differences in thickness in Table 1 are likely caused by variations in dehydration properties associated with the different tissue types present in Fig. 5(d).

The major element and thickness data in Table 1 were subsequently used as matrix data for each tissue region in GeoPIXE and used to determine the mass density of Ca in the ex vivo tissue. The Ca hot-spot regions had a geometric size that was too small (20–50 μm) to produce statistically reliable matrix compositions. In this case, the matrix was taken to correspond to a large area of outer epithelium tissue without Ca hot-spots. Even in the Ca hot spots the Ca concentration was so small that it did not significantly influence the stopping cross section factors. Subsequently, for each of the regions, (including the Ca hotspots) the Ca molarity was determined using Eq. (7). The results are presented in Fig. 10.

4.2. Measurement uncertainties

The stochastic uncertainties in the major element composition (Table 1) and Ca molarity (Fig. 10) measurements originate from statistical counting errors in the PIXE, EBS, OA-STIM measurements, Y (Eq. (6), Section 3.2), and an estimated $\pm 2\%$ uncertainty in determining ΔE_1 . The ratio of the stopping cross section factors also introduces variation originating from the compositional uncertainty. In the case of the Ca molarity, an additional source of stochastic uncertainty is variations in the local thickness of the frozen tissue section. These variations were taken to be $\pm 10\%$ of the film thickness. The counting statistical uncertainties were taken from the fitting codes and the uncertainties in Table 1 and the error bars in Fig. 10 were ascertained using standard error propagation formulae.

Systematic uncertainties originate from; (i) stopping cross sections, (ii) deviations from Bragg's rule in (i), (iii) uncertainties in the EBS scattering cross sections (iv) uncertainty in the tissue section thickness and (v) the dry tissue density. (i) The DPASS stopping cross section

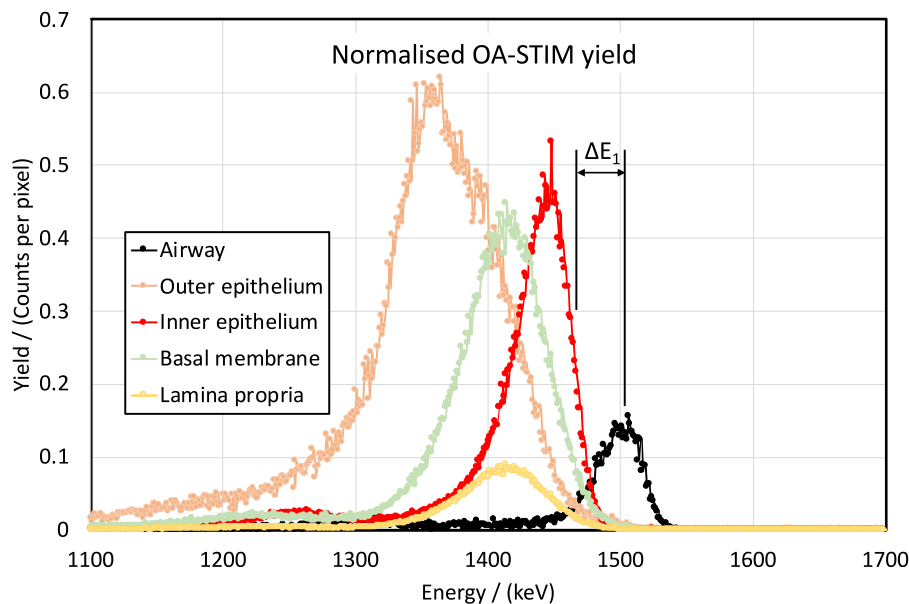


Fig. 7. Normalised hydrogen OA-STIM energy spectra for the different tissue regions delineated in Fig. 6(b).

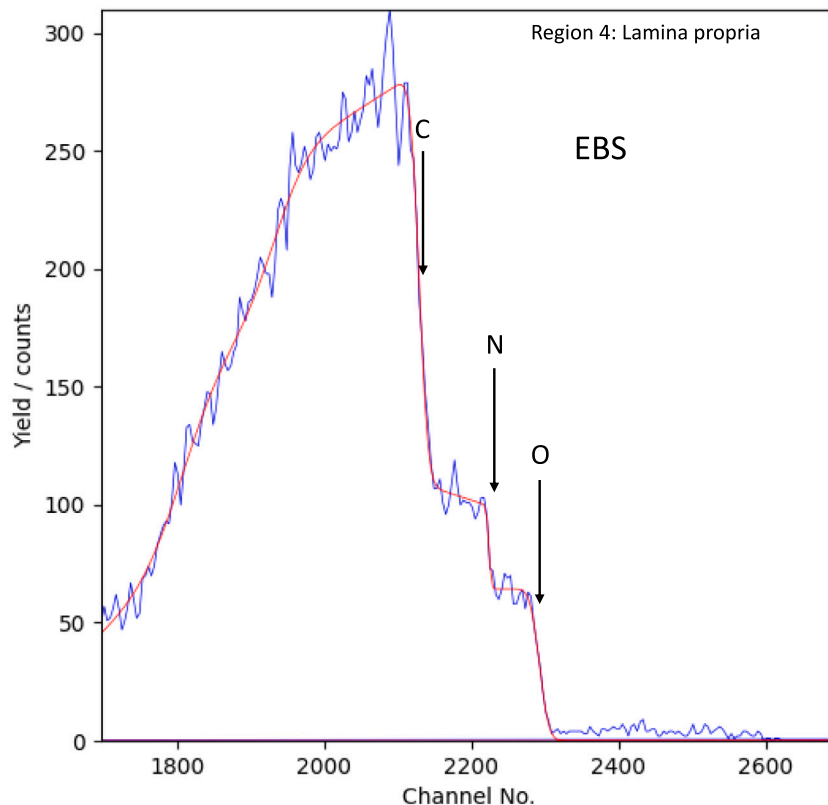


Fig. 8. EBS energy spectra from the lamina propria region. The blue and red lines correspond to the raw experimental and fit used to determine the surface edge heights.

predictor values [39,40,46] were used which are presumed to have negligible departure from the true value. (ii) The stopping cross sections for biological targets may exhibit small departures from Bragg's rule ($\lesssim 2\%$) because their average atomic number is small. The effects of (i) and (ii) will be small on the composition and molarity since they enter into the calculations as ratios of stopping cross section factors (e.g. in Eq. (5)). (iii) The p-C, p-N and p-O backscattering cross sections from SigmaCalc [37,38] represent an empirical prediction. Comparison of SigmaCalc cross sections with published experimental

data suggests the uncertainties are a few % for 2 MeV protons. The systematic uncertainty in the mean frozen section thickness (iii) is governed by the cryomicrotome design and precision. For modern rotary cryomicrotomes the slice thickness accuracy is better than 5%. The resulting molarity uncertainty is smaller than the stochastic uncertainties in Fig. 10. (iv) The dry tissue density is an ill-determined quantity with little published data. Although, for convenience, it was used in the input data for the PIXE data analysis, the value did not influence Ca to matrix dry mass ratio nor the areal density and hence

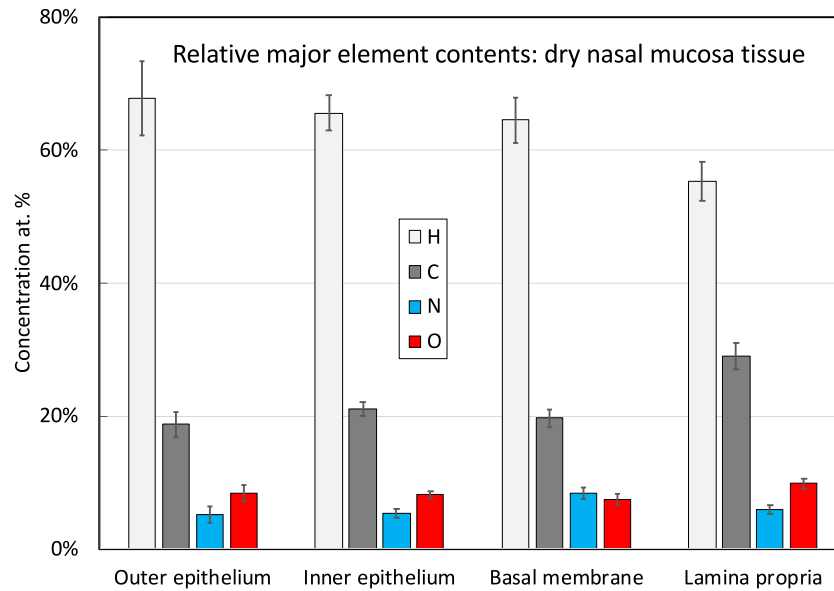


Fig. 9. Major element composition of dry nasal mucosa tissue. The error bars denote counting statistical uncertainties.

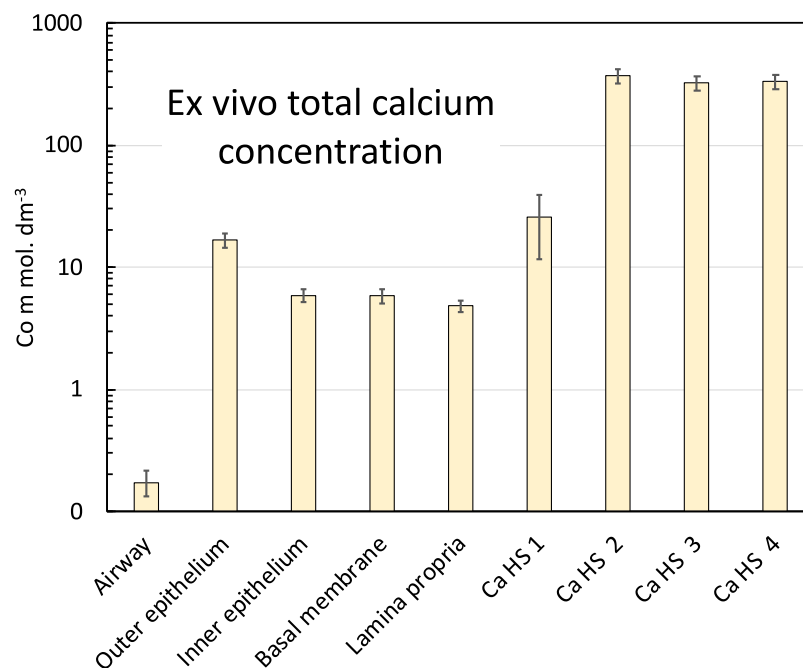


Fig. 10. Ca molarities for ex vivo nasal mucosa for different tissue regions and four Ca hot-spots (Ca HS 1 to Ca HS 4). The uncertainties represent the stochastic statistical uncertainties combined. (See text.)

did not affect the measured molarity (Eq. (7)). However, the dry tissue density did contribute a systematic uncertainty to the measured dry tissue section thickness of Table 1. A further uncertainty originates from geometric thickness variations in the dry tissue film due to differential stresses during lyophilisation that result from differences in tissue morphology. Regions with enhanced thickness due to localised curling of the dry tissue would have both an increased thickness and an unchanged hydrogen atomic fraction (from Eqs. (3),(5) and (7)). While such an enhancement was observed in the PIXE map for S it was not observed for P (Fig. 5(a)) and hence thickness variation due to curling could be ruled out.

4.3. Sequestration of Ca

The measurement method is completely blind to the oxidation state of Ca and measures the total Ca concentration. Bearing in mind that, as noted in the introduction, under normal homeostasis conditions there is a dynamic equilibrium between the bound Ca and Ca^{2+} . The total Ca concentration must then exceed that of Ca^{2+} . Ca^{2+} is an important signal substance that is implicated in the release of mucus from goblet cells [12,18,47], contraction of muscles and cilli, apoptosis, functions in the brain, transport of nerve impulses, as well as inflammation and activation of the immune system. Normal physiological levels for Ca^{2+}

under homeostasis conditions lie in the range 0.3–2 mmol. dm⁻³ [7–9,11,48,49]. Soft tissues are not generally specialised in storage of Ca in mineralisations but will store Ca by binding to proteins. Consequently, the measured levels of total Ca in the different tissue regions can be considered unremarkable.

The enhanced Ca in the hot spots seen in the inner epithelium (Fig. 5) are ~2–25 times greater than that of the surrounding outer epithelial tissue (Fig. 10) which is itself elevated ~2 times above inner epithelium and other tissues. The total Ca levels, at least for, Ca HS 2, 3 and 4 lie in the range 200–400 mmol dm⁻³. While the Ca molarity in the hot spots is clearly elevated, it is far below that of the level corresponding to the Ca molarity for bone tissue (~9.7 mol. dm⁻³, derived from the ICRU composition data [5] for human cortical bone). Although the concentration of sequestered Ca in mineralisations need not be as high as for bone tissue, if it were the result of deposition of calcium hydroxyapatite, P with Ca would be colocalised in the hot spots. Reference to Fig. 5 showed this is not the case. Deposition of airborne calcium bearing particulate matter on the outer epithelium cannot be entirely excluded but can be considered unlikely. The subject was kept in a strictly controlled ABSL-2 environment and was fed standard monkey chow which is enriched in calcium and other minerals. Nasal ingestion of food would give rise to concentration hot-spots for the other enriched elements, which was not observed. The elevated concentration of Ca in the hot spots and outer epithelium could be associated with a high density of goblet cells. The goblet cells produce mucus, which is composed of 90–95 mass % water with mucus glycoproteins as the other major constituent which gives mucus its visco-elastic character [12]. This composition is believed to be optimal for removal of particles and debris [47]. Goblet cells contain granules of highly compressed (100–200 fold) mucins [12] containing large numbers of Ca²⁺ ions. (Loss of these ions by out-diffusion when exposed to the low ~6 mmol. dm⁻³ intracellular Ca concentration leads to a rapid release of expanded mucin molecules by Coulombic expansion [12].) Such a high degree of volume compression of Ca-loaded mucins in the granules of goblet cells could account for similar localised total Ca molarities to that observed in the hot spots as well as in the outer epithelium.

Like Ca, the PIXE signals for S is enhanced in the outer epithelium (Fig. 5(b)), whereas P (Fig. 5(a)) is enhanced in both the inner and outer epithelium. We previously observed a similar differentiation of P and S in the outer villi of jejunum tissue of a SIV infected macaque [27]. It is notable glycoproteins contain little or no S in their structure. Hence, the S enhancement seen in the outer epithelium (Fig. 5(b)) is unlikely to be associated with mucus glycoproteins in the granules of goblet cells (Fig. 1 of Ref. [12]). On the other hand, in the epithelium the columnar cells with cilia are rich in structural proteins such as tubulins and dyneins [3] that might contribute to an enhanced S content.

5. Conclusions

Simultaneous Off-Axis Scanning Transmission Ion Microscopy (OA-STIM), Particle Induced X-ray Emission (PIXE) and Elastic Backscattering Spectrometry (EBS) have been employed to determine the Ca molarity for ex-vivo nasal mucosa tissue from tissue sections. High Ca concentrations in hot-spots were observed in the outer epithelium with Ca concentrations that significantly exceeded the levels in surrounding tissues. The Ca concentrations that were within the normal physiological range for Ca. The sequestration of Ca in concentrated hotspots is unlikely to be of environmental origin and more likely due to either calcification in the outer epithelial tissue or Ca sequestration by goblet cells of condensed mucins.

Declaration of competing interest

The authors declare that they have no known competing financial interests or personal relationships that could have appeared to influence the work reported in this paper.

Acknowledgements

The project was supported by the The Office of the Vice President for Research, Innovation, and Economic Development of the University of Louisiana at Lafayette. Accelerator operation in Uppsala is supported by the Swedish Research Council VR-RFI (Contracts No. 2017-00646_9 and 2019-00191) and the Swedish Foundation for Strategic Research (Contract No. RIF14-0053). HJW acknowledges support from The Research Council of Norway for the Norwegian Micro and Nano-Fabrication Facility, NorFab (Project 11 No. 245963).

References

- [1] P. Chellan, P.J. Sadler, The elements of life and medicines, *Phil. Trans. Royal Soc. A: Math., Phys. Eng. Sci.* 373 (2037) (2015) 20140182, <http://dx.doi.org/10.1098/rsta.2014.0182>, URL <https://royalsocietypublishing.org/doi/abs/10.1098/rsta.2014.0182>.
- [2] H.J. Whitlow, M.-Q. Ren, in: M. Nastasi, J.W. Mayer, Y. Wang (Eds.), *Ion Beam Analysis: Fundamentals and Applications*, CRC Press, Taylor & Francis Group, Boca Raton FL, 33487, USA, 2015, pp. 309–337.
- [3] E.N. Marieb, *Human Anatomy & Physiology*, sixth ed., Pearson Benjamin Cummings, 2004.
- [4] C.M. Weaver, Calcium, in: B.P. Marriott, D.F. Birt, V.A. Stallings, A.A. Yates (Eds.), *Present Knowledge in Nutrition (Eleventh Edition)*, Eleventh ed., Academic Press, 2020, pp. 321–334, <http://dx.doi.org/10.1016/B978-0-323-66162-1.00019-6>, URL <https://www.sciencedirect.com/science/article/pii/B9780323661621000196>.
- [5] ICRU, *Stopping powers for electrons and positrons*, Tech. Rep. No. 37, International Commission on Radiation Units and Measurements, 1984.
- [6] P.A. Hasgall, F.D. Gennaro, C. Baumgartner, B.L. E. Neufeld, M.C. Gosselin, D. Payne, A. Klingeböck, N. Kuster, IT'IS Database for thermal and electromagnetic parameters of biological tissues, 2022, <http://dx.doi.org/10.13099/VIP21000-04-1.itis.swiss/database>.
- [7] M. Vig, J.-P. Kinet, Calcium signaling in immune cells, *Nat. Immunol.* 10 (1) (2009) 21–27, <http://dx.doi.org/10.1038/ni.f.220>.
- [8] Y.-J. Park, S.-A. Yoo, M. Kim, W.-U. Kim, The role of calcium–calcineurin–NFAT signaling pathway in health and autoimmune diseases, *Front. Immunol.* 11 (2020) 195, <http://dx.doi.org/10.3389/fimmu.2020.00195>, URL <https://www.frontiersin.org/article/10.3389/fimmu.2020.00195>.
- [9] Y. Ingelbert, J. Ajadef, D. Debanne, Synaptic plasticity rules with physiological calcium levels, *Proc. Natl. Acad. Sci. USA* 117 (52) (2020) 33639–33648, URL <https://www.pnas.org/doi/full/10.1073/pnas.2013663117>.
- [10] D. Proudfoot, Calcium signaling and tissue calcification, *Cold Spring Harb Perspect. Biol.* 11 (2019) a035303, <http://dx.doi.org/10.1101/cshperspect.a035303>.
- [11] A.H. Rossi, W.C. Salmon, M. Chua, C.W. Davis, Calcium signaling in human airway goblet cells following purinergic activation, *Am. J. Physiol.-Lung Cell. Mol. Physiol.* 292 (1) (2007) L92–L98, <http://dx.doi.org/10.1152/ajplung.00081.2006>, PMID: 16951133.
- [12] R. Bansil, B.S. Turner, The biology of mucus: Composition, synthesis and organization, *Adv. Drug Deliv. Rev.* 124 (2018) 3–15, <http://dx.doi.org/10.1016/j.addr.2017.09.023>, Technological strategies to overcome the mucus barrier in mucosal drug delivery, URL <https://www.sciencedirect.com/science/article/pii/S0169409X17302041>.
- [13] M.-Q. Ren, Y.-T. Zhou, H.-X. Chen, T.-Y. Li, S.K. Vajandar, T. Osipowicz, F. Watt, C.-W. Li, Quantitative analysis of multiple elements in healthy and remodeled epithelium from human upper airway mucosa using nuclear microscopy, *Allergy* 73 (3) (2018) 724–727, <http://dx.doi.org/10.1111/all.13329>.
- [14] P.J. Santangelo, K.A. Rogers, C. Zurla, E.L. Blanchard, S. Gumber, K. Strait, F. Connor-Stroud, D.M. Schuster, P.K. Amancha, J.J. Hong, S.N. Byrreddy, J.A. Hoxie, B. Vidakovic, A.A. Ansari, E. Hunter, F. Villinger, Whole-body immunoPET reveals active SIV dynamics in viremic and antiretroviral therapy-treated macaques, *Nature Methods* 12 (5) (2015) 427–432, <http://dx.doi.org/10.1038/nmeth.3320>.
- [15] H. Puchler, S.N. Meloan, M.S. Terry, On the history and mechanism of Alizarin and Alizarin red S stains for calcium, *J. Histochemistry & Cytochemistry* 17 (2) (1969) 110–124, <http://dx.doi.org/10.1177/17.2.110>, PMID: 4179464.
- [16] J. Pallon, C. Ryan, N. Arteaga Marrero, M. Elfman, P. Kristiansson, E. Nilsson, C. Nilsson, STIM evaluation in GeoPIXE to complement the quantitative dynamic analysis, *Nucl. Instrum. Methods Phys. Res. B* 267 (12) (2009) 2080–2084, <http://dx.doi.org/10.1016/j.nimb.2009.03.036>, Proceedings of the 11th International Conference on Nuclear Microprobe Technology and Applications and the 3rd International Workshop on Proton Beam Writing, URL <https://www.sciencedirect.com/science/article/pii/S0168583X09003486>.

- [17] J. Pallon, V. Auzelyte, M. Elfman, M. Garmer, P. Kristiansson, K. Malmqvist, C. Nilsson, A. Shariff, M. Wegdén, An off-axis STIM procedure for precise mass determination and imaging, *Nucl. Instrum. Methods Phys. Res. B* 219–220 (2004) 988–993, <http://dx.doi.org/10.1016/j.nimb.2004.01.201>, URL <https://www.sciencedirect.com/science/article/pii/S0168583X04002514>, Proceedings of the Sixteenth International Conference on Ion Beam Analysis.
- [18] P. Aguer, L. Alves, P. Barberet, E. Gontier, S. Incerti, C. Michelet-Habchi, Z. Kertész, A. Kiss, P. Moretto, J. Pallon, T. Pinheiro, J. Surlève-Bazeille, Z. Szikszai, A. Verissimo, M. Ynsa, Skin morphology and layer identification using different STIM geometries, *Nucl. Instrum. Methods Phys. Res. B* 231 (1) (2005) 292–299, <http://dx.doi.org/10.1016/j.nimb.2005.01.073>, Nuclear Microprobe Technology and Applications, URL <https://www.sciencedirect.com/science/article/pii/S0168583X05000935>.
- [19] G. Bench, P.G. Grant, D. Ueda, S.S. Cliff, K.D. Perry, T.A. Cahill, The use of STIM and PESA to measure profiles of aerosol mass and hydrogen content, respectively, across mylar rotating drums impactor samples, *Aerosol Sci. Technol.* 36 (5) (2002) 642–651, <http://dx.doi.org/10.1080/02786820252883874>.
- [20] M. Chiari, G. Calzolari, M. Giannoni, F. Lucarelli, S. Nava, S. Becagli, Use of proton elastic scattering techniques to determine carbonaceous fractions in atmospheric aerosols collected on Teflon filters, *J. Aerosol Sci.* 89 (2015) 85–95, <http://dx.doi.org/10.1016/j.jaerosci.2015.07.006>, URL <https://www.sciencedirect.com/science/article/pii/S0021850215001123>.
- [21] J. Voltr, J. Král, Z. Nejedlý, PESA as a complementary tool to PIXE at CTU Prague, *Nucl. Instrum. Methods Phys. Res. B* 150 (1) (1999) 554–558, [http://dx.doi.org/10.1016/S0168-583X\(98\)00951-3](http://dx.doi.org/10.1016/S0168-583X(98)00951-3), URL <https://www.sciencedirect.com/science/article/pii/S0168583X98009513>.
- [22] N.T. Deoli, A.B. de Vera, K.L. Coutee, J.D. Dias, H.E. Udeogu, S. Banerjee, P.L. Klerks, W.A. Hollerman, K.H. Hasenstein, Status of the Louisiana accelerator center, *AIP Conf. Proc.* 2160 (1) (2019) 040005, <http://dx.doi.org/10.1063/1.5127685>, URL <https://aip.scitation.org/doi/abs/10.1063/1.5127685>.
- [23] G. Nagy, H.J. Whitlow, D. Primetzhofer, The scanning light ion microprobe in Uppsala – status in 2022, *Nucl. Instrum. Methods Phys. Res. B* 533 (2022) 66–69, <http://dx.doi.org/10.1016/j.nimb.2022.10.017>, URL <https://www.sciencedirect.com/science/article/pii/S0168583X22003007>.
- [24] C. Ryan, Developments in Dynamic Analysis for quantitative PIXE true elemental imaging, *Nucl. Instrum. and Meth. B* 181 (1) (2001) 170–179, [http://dx.doi.org/10.1016/S0168-583X\(01\)00374-3](http://dx.doi.org/10.1016/S0168-583X(01)00374-3), URL <https://www.sciencedirect.com/science/article/pii/S0168583X01003743>.
- [25] C. Ryan, D. Jamieson, C. Churms, J. Pilcher, A new method for on-line true elemental imaging using PIXE and the proton microprobe, *Nucl. Instrum. Meth. B* 104 (1) (1995) 157–165, [http://dx.doi.org/10.1016/0168-583X\(95\)00404-1](http://dx.doi.org/10.1016/0168-583X(95)00404-1), URL <https://www.sciencedirect.com/science/article/pii/S0168583X95004041>.
- [26] C.G. Ryan, Quantitative trace element imaging using PIXE and the nuclear microprobe, *Int. J. Imaging Syst. Technol.* 11 (4) (2000) 219–230, <http://dx.doi.org/10.1002/ima.1007>, URL <https://onlinelibrary.wiley.com/doi/abs/10.1002/ima.1007>, arXiv:<https://onlinelibrary.wiley.com/doi/pdf/10.1002/ima.1007>.
- [27] H.J. Whitlow, N.T. Deoli, A. de Vera, K. Morgan, F. Villinger, Heavy elements revealed in Jejunum of Simian immunodeficiency virus infected monkeys by microparticle induced X-Ray emission, *Phys. Status Solidi (A)* 218 (1) (2021) 2000107, <http://dx.doi.org/10.1002/pssa.202000107>, URL <https://onlinelibrary.wiley.com/doi/abs/10.1002/pssa.202000107>.
- [28] S. Leary, et al., AVMA Guidelines for the Euthanasia of Animals: AVMA Guidelines for the Euthanasia of Animals: 2020 Edition, Tech. Rep., American Veterinary Medical Association, 1931 N. Meacham Road Schaumburg, IL 60173, USA, 2020, pp. 33–34.
- [29] Safety Data sheet Tissue-Tek® O.C.T. Compound, Sakura Finetek USA Inc., 1750 West 214th St. Torrance, CA 90501, USA, 2016.
- [30] M.-Q. Ren, Nuclear Microscopy: Development and applications in Atherosclerosis, Parkinsons Disease and Materials Physics (Ph.D. thesis), University of Jyväskylä, Faculty of Mathematics and Natural Sciences, Jyväskylä, Finland, 2007.
- [31] H. Whitlow, G. Possnert, C.S. Petersson, Quantitative mass and energy dispersive elastic recoil spectrometry: Resolution and efficiency considerations, *Nucl. Instrum. Methods: Sec. B* 27 (1987) 448.
- [32] M. Nastasi, J.W. Mayer, Y. Wang (Eds.), *Ion Beam Analysis: Fundamentals and Applications*, CRC Press, Taylor & Francis Group, Boca Raton FL, 33487, USA, 2015.
- [33] W.-K. Chu, J.W. Mayer, M.-A. Nicolet, *Backscattering Spectrometry*, Academic Press, New-York, 1978.
- [34] A. Gurbich, Evaluation of non-Rutherford proton elastic scattering cross section for carbon, *Nucl. Instrum. Methods Phys. Res. B* 136–138 (1998) 60–65, [http://dx.doi.org/10.1016/S0168-583X\(97\)00837-9](http://dx.doi.org/10.1016/S0168-583X(97)00837-9), Ion Beam Analysis, URL <https://www.sciencedirect.com/science/article/pii/S0168583X97008379>.
- [35] A. Gurbich, Evaluation of non-Rutherford proton elastic scattering cross section for nitrogen, *Nucl. Instrum. Methods Phys. Res. B* 266 (8) (2008) 1193–1197, <http://dx.doi.org/10.1016/j.nimb.2007.11.026>, Ion Beam Analysis, URL <https://www.sciencedirect.com/science/article/pii/S0168583X07017235>.
- [36] A. Gurbich, Evaluation of non-Rutherford proton elastic scattering cross section for oxygen, *Nucl. Instrum. Methods Phys. Res. B* 129 (3) (1997) 311–316, [http://dx.doi.org/10.1016/S0168-583X\(97\)00288-7](http://dx.doi.org/10.1016/S0168-583X(97)00288-7), URL <https://www.sciencedirect.com/science/article/pii/S0168583X97002887>.
- [37] A. Gurbich, SigmaCalc recent development and present status of the evaluated cross-sections for IBA, *Nucl. Instrum. Methods Phys. Res. B* 371 (2016) 27–32, <http://dx.doi.org/10.1016/j.nimb.2015.09.035>, The 22nd International Conference on Ion Beam Analysis (IBA 2015), URL <https://www.sciencedirect.com/science/article/pii/S0168583X15008940>.
- [38] A. Gurbich, SigmaCalc, 2015, URL <http://sigmacalc.iate.obninsk.ru>.
- [39] P. Sigmund, A. Schinner, Binary theory of electronic stopping, *Nucl. Instrum. Methods Phys. Res. B* 195 (1) (2002) 64–90, [http://dx.doi.org/10.1016/S0168-583X\(01\)01162-4](http://dx.doi.org/10.1016/S0168-583X(01)01162-4), URL <https://www.sciencedirect.com/science/article/pii/S0168583X01011624>.
- [40] A. Schinner, P. Sigmund, Expanded PASS stopping code, *Nucl. Instrum. Methods Phys. Res. B* 460 (2019) 19–26, <http://dx.doi.org/10.1016/j.nimb.2018.10.047>, Special Issue: SHIM-ICACS Swift Heavy Ions in Matter and International Conference on Atomic Collisions in Solids, 1–7 July 2018 Caen, France, URL <https://www.sciencedirect.com/science/article/pii/S0168583X18306396>.
- [41] R. Jennings, C. Premandan, Veterinary Histology, The Ohio State University, 2017, URL <https://ohiostate.pressbooks.pub/vethisto/chapter/2-epithelium-intro/>.
- [42] L. Uraih, R. Maronpot, Normal histology of the nasal cavity and application of special techniques, *Environ. Health Perspect.* 85 (1990) 187–208, <http://dx.doi.org/10.1289/ehp.85-1568325>, URL <https://europemc.org/articles/PMC1568325>.
- [43] K. Gul, K. Shahzad, J. Taj, A. Awais, J. Hussain, F. Qureshi, N. Ali, Experimental study of proton scattering on carbon, *Nucl. Instrum. Methods Phys. Res. B* 269 (18) (2011) 2032–2034, <http://dx.doi.org/10.1016/j.nimb.2011.06.006>, URL <https://www.sciencedirect.com/science/article/pii/S0168583X1100591X>.
- [44] H. Whitlow, G. Nagy, Proton beam induced degradation of Pioloform® (polyvinyl butyral (PVB)) support films used for analysis of biomedical tissue sections, *Nucl. Instrum. Methods: Sec. B* Accepted (2022) <http://dx.doi.org/10.1016/j.nimb.2023.03.028>, This conference.
- [45] M.K. Aliev, P. Dos Santos, J.A. Hoerter, S. Soboll, A.N. Tikhonov, V.A. Saks, Water content and its intracellular distribution in intact and saline perfused rat hearts revisited, *Cardiovasc. Res.* 53 (1) (2002) 48–58, [http://dx.doi.org/10.1016/S0008-6363\(01\)00474-6](http://dx.doi.org/10.1016/S0008-6363(01)00474-6), arXiv:<https://academic.oup.com/cardiovasres/article-pdf/53/1/48/1197620/53-1-48.pdf>.
- [46] P. Sigmund, A. Schinner, DPASS, 2020, URL <https://www.sdu.dk/en/dpass>.
- [47] D.F. Rogers, Airway goblet cells: Responsive and adaptable front-line defenders, *Eur. Respir. J.* 7 (9) (1994) 1690–1706.
- [48] E.N. Marieb, *Human Anatomy & Physiology*, sixth ed., Pearson Benjamin Cummings, 2004, pp. 1042–1047.
- [49] G.V. Drake T. M., Calcium, URL <https://www.ncbi.nlm.nih.gov/books/NBK557683/>.